Hindawi
International Journal of Antennas and Propagation
Volume 2021, Article ID 9984595, 15 pages
https://doi.org/10.1155/2021/9984595

Research Article

Electromagnetic Shielding Techniques in the Wireless Power Transfer System for Charging Inspection Robot Application

Chaoqun Jiao,[1] **Yang Xu**,[1] **Xiang Li**,[1] **Xiumin Zhang**,[1] **Zhibin Zhao**,[2] **and Chengzong Pang**[3]

[1]*School of Electrical Engineering, Beijing Jiaotong University, Beijing 100044, China*
[2]*State Key Laboratory of Alternate Electrical Power System with Renewable Energy Sources, North China Electric Power University, Beijing 102206, China*
[3]*Department of Electrical Engineering and Computer Science, Wichita State University, Wichita, KS, USA*

Correspondence should be addressed to Chaoqun Jiao; chqjiao@bjtu.edu.cn and Yang Xu; 17117425@bjtu.edu.cn

Received 9 March 2021; Revised 6 May 2021; Accepted 12 June 2021; Published 5 July 2021

Academic Editor: Giuseppina Monti

Aiming at eliminating the leakage of magnetic fields from the wireless power transfer (WPT) system, the structural and working characteristics of the WPT system for the inspection robot are analyzed and an electromagnetic shielding method combining passive shielding and active shielding is proposed in this paper. Firstly, we simulated the magnetic field distribution of the WPT system in Maxwell. Secondly, passive shielding is configured in the WPT system, and the material, size, and position of the passive shielding are studied. Then, we add active shielding to areas where passive shielding cannot achieve a good shielding effect. Based on the analysis and summary of the two methods, we shield the WPT system in the horizontal direction with the appropriate size and distance of aluminum plate, and in the vertical direction, we use the active shielding coils. Simulation and experimental results show that the scheme only slightly reduces the transmission efficiency of the system (from 80.2% to 77.6%), but the shielding ability is 34.06% higher than that of only aluminum plates. The excellent effect of the proposed shielding method is verified in our experiment.

1. Introduction

The traditional wired charging technology is still the main way of power transmission at present, and the power transmission is realized by the physical connection of plug and socket. However, it also has a variety of problems, such as safety problems caused by abrasion and aging, the inconvenience of charging portable electronic equipment and implantable medical equipment, and the danger of power transmission in mine and underwater working environments. Wireless charging technology, as a new power transmission mode, can effectively realize noncontact power transmission and meet the needs of safety, efficiency, and convenience in some specific scenarios.

Because the WPT system needs to use the magnetic coupling mechanism to transmit energy with the high-frequency magnetic field (MF), the electromagnetic radiation problem will bring panic to the public and even a real security threat [1–3].

Inspection robot is the product of power system automation in recent years. Its working environment is complex. The traditional charging mode of the power supply line and electric shock occupies its working time and reduces production efficiency. The wireless charging strategy allows the inspection robot to complete the inspection task along a specific track and replenish electric energy. However, the inspection robot will have an adverse effect on the electromagnetic environment during wireless charging, so it is necessary to design a shielding method for the WPT system.

Passive shielding is a common electromagnetic shielding strategy. Passive shielding refers to the optimization of the magnetic channel by using the magnetic conductivity of magnetic materials or the formation of reverse MF by eddy current produced by conductive metal materials in high-frequency MF, so as to suppress the leakage of MF [4–6]. Attaching an aluminum (Al) plate to the transmit (Tx) coil and/or the receive (Rx) coil is the most prevalent measure,

which exploits the eddy current induced in the high-conductivity metal to block the leakage field. For stationary electric vehicle (EV) wireless charging applications, regardless of whether the coil structure is a basic circular pad [7], DD pad [8, 9], DDQ pad [10], or even bipolar pad [11], the Al-plate passive shielding [12–14] is widely used.

Active shielding is relatively novel, but it can also play a good shielding effect in the WPT system. In some cases with a large air gap, the leakage MF in the horizontal direction cannot be ignored. The suppression coil with excitation source produces the offset MF opposite to the original MF to clear or weaken the leakage MF [6, 15–17]. The shielding effect is obvious in a dynamic wireless charging system, but this method is unfavorable to the overall efficiency of the system, so it is necessary to design a suitable shielding scheme [18, 19].

Previous studies to reduce the EMF by using ferrite tile or another material to cover the WPT system are heavy and cause additional costs [20]. And those works by using shielding coil lack experimental verification usually [21, 22]. Moreover, the coil form of the WPT system is limited to flat type in previous works, and the research on electromagnetic shielding of I-shaped WPT system is lacking. In this paper, we use Simplorer and Maxwell to conduct a field-circuit cosimulation for the WPT system at first. On this basis, the corresponding shielding scheme is designed according to the magnetic field distribution characteristics of the primary side and secondary side, and the advantages of passive and active shielding in the scheme are fully utilized. Afterward, the position, material, and size of the shielding device are discussed and optimized. Our research shows that the vertical shield at the receiving side is more favorable to reduce the magnetic field around the system, and the active shielding coil is better than the aluminum plate in the vertical direction. The simulation and experimental results show that the method can effectively reduce the adverse effects on the electromagnetic environment during the working process of the magnetic coupling mechanism and ensure the working efficiency of the system.

2. Magnetic Coupling Mechanism of the Inspection Robot

2.1. Selection of the Secondary Coil. According to the working characteristics of the slow-moving inspection robot, its resonant coil should be designed in accordance with the requirements of dynamic wireless charging. The secondary coil is located under the robot chassis. Due to the limited installation area of the robot chassis, space must be used as much as possible, and the skin effect, eddy current effect, magnetic saturation, and other factors must be fully considered to obtain a higher coupling coefficient and transmission efficiency. For the selection of resonant coils, there are more research studies on the flat circular, E-type magnetic core skeleton, double D type, and so on [13]. The flat circular shape is used as the secondary side although it can be charged efficiently under ideal conditions facing the primary side, but considering that the installable area of the actual inspection robot is a rectangular space of about 300 mm × 150 mm, the design size of this shape will be limited and the charging effect will be greatly reduced. As the secondary side, the E-shaped core frame can be designed to be rectangular with multiple windings. The core frame used can also improve the antioffset ability of the coil, but the structure is bulky and difficult to flatten the design. Double D type is formed by two circular coils connected in reverse series, generating MF in opposite directions. Figure 1 shows the effect diagram of different winding methods on the secondary side. Compared with the other two coils, double D winding is lighter and has a larger coupling coefficient and stronger antioffset ability.

2.2. Selection of the Primary Coil. As to the primary side of the dynamic wireless charging system, early studies have adopted the long rail type and the segmented rail type. The long rail type is characterized by its simple coil structure, but it is restricted by the length of the rail when designing the size, number of turns, and self-inductance. It is not flexible enough and is not suitable for scenarios with long charging lines. Segmented guide rails make up for the shortcomings of long guide rails, and the combination method is flexible, but each part requires independent compensation devices and switch control strategies, and the system is more complicated and costly. This paper adopts the primary coil layout of the I-shaped magnetic core skeleton shown in Figure 2. The two magnetic cores are a set, the Litz wire is wound on the skeleton clockwise and counterclockwise in the driving direction, and the size and winding method of the secondary side are the same. Correspondingly, this double-magnetic-pole coupling mechanism has the following advantages:

(1) The coils on a single set of magnetic poles are arbitrarily superimposed within the range of the magnetic pole height, which can increase the inductance and improve the vertical transmission capacity

(2) Since the primary coil needs to be buried below the ground, the H-shaped coil has a narrow width, which is beneficial to reduce the track excavation width

(3) It has the characteristic of modularization, connecting multiple groups of primary coils with wires, which can extend the inspection path and facilitate troubleshooting

(4) The adjacent magnetic poles wind in opposite directions so that the polarity of the magnetic induction intensity B of each pole is reversed according to the current direction. Therefore, the main magnetic flux circulates between the nearest poles to form a closed MF and reduce the leakage MF around the power rail

2.3. Analysis of the Equivalent Circuit. According to the different numbers and composition modes of resonant capacitors and inductors, the tuning circuit of the wireless charging system can be divided into four basic resonant topologies and six composite topologies. Among them,

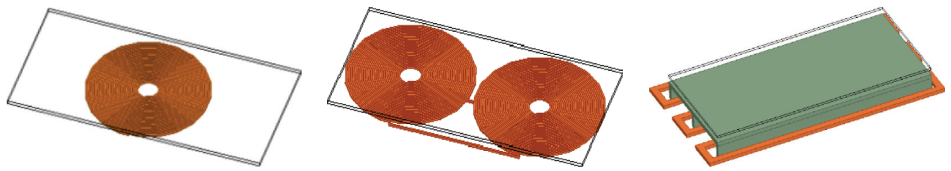

Figure 1: Effect diagram of different winding methods on the secondary side. (a) Flat circular winding. (b) Double D winding. (c) E-type core skeleton winding.

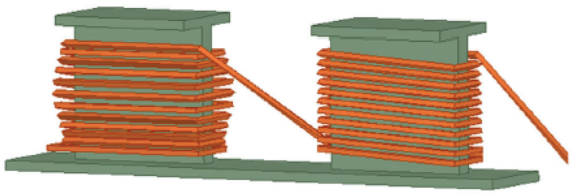

Figure 2: Effect diagram of I-shaped magnetic core skeleton coil on the primary side.

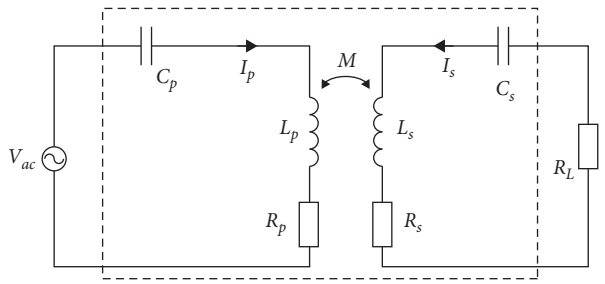

Figure 3: Impedance model of SS type compensation structure.

the series-series (SS) compensation topology is simple in structure and convenient in parameter design. It is suitable for the voltage type system in this study. The impedance model of the compensation structure is shown in Figure 3.

L_p and L_s are the inductances of the primary coil and secondary coil; meanwhile, C_p and C_s are the resonant capacitances of L_p and L_s. R_p and R_s represent coil resistances. Because of the large transmission air gap, the primary and secondary sides are weakly coupled, and the secondary side is reduced to the primary side in the form of reflected impedance.

2.4. Simulation of the Magnetic Coupling Mechanism. We use the finite element simulation software ANSYS to simulate the ideal working environment of the system. Figure 4 shows the situation where the primary coil and the secondary coil are completely aligned. The charging guide line is long, and only a small section is selected for modeling. According to the robot's chassis size, launch track size, and transmission requirements, the selected resonant coil parameters are as follows: the number of turns of the double D coil on the secondary side is 24 mm × 2 mm; using the dense winding method, the total length is 300 mm; the total width is 150 mm; the transmitter side is H type. The number of turns of the coil is 16 mm × 2 mm, and the dense winding method is also adopted. The total length is 300 mm, the total width is 100 mm, and the total height is 55 mm; the closest air gap between the primary side and the secondary side is 50 mm.

We select a horizontal observation line 1 which is 50 mm above the secondary side with a length of 300 mm and a vertical observation line 2 which is 50 mm to the right of the secondary coil and 200 mm above the ground for observation (the plane with $Z = -50$ mm is specified as the ground). Because there are communication, control, and other hardware equipment 50 mm above the secondary side,

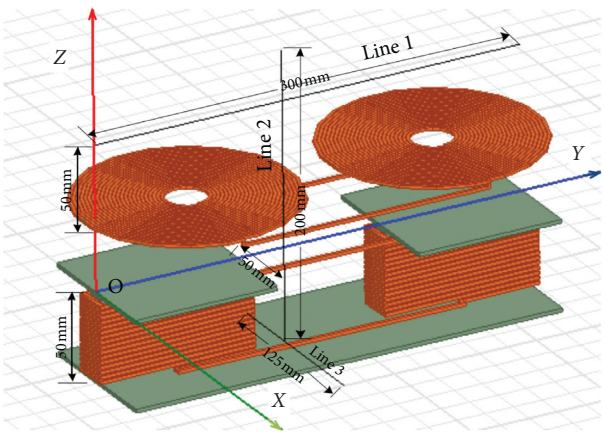

Figure 4: Simulation model of wireless charging magnetic coupling mechanism.

there may be electrical equipment being inspected and maintenance workers 50 mm to the right of the secondary side. These areas need to be protected. In addition, a horizontal observation line 3 with a length of 125 mm is set on the right side of the primary coil, which is used to grasp the spread of the MF above the ground. Observing the distance from the resonant coil can ensure that there is no electromagnetic interference. Using Simplorer and Maxwell to conduct field-circuit cosimulation, when the magnetic coupling mechanism is under the rated operating conditions of 2 kW and 85 kHz, the simulation results of each observation line are shown in Figure 5. According to ICNIRP [23, 24], the magnetic induction intensity in the nonworking area of the magnetic coupling mechanism seriously exceeds the standard, and shielding measures are needed to reduce the magnetic induction intensity in the designated area to the limit of 27 μT.

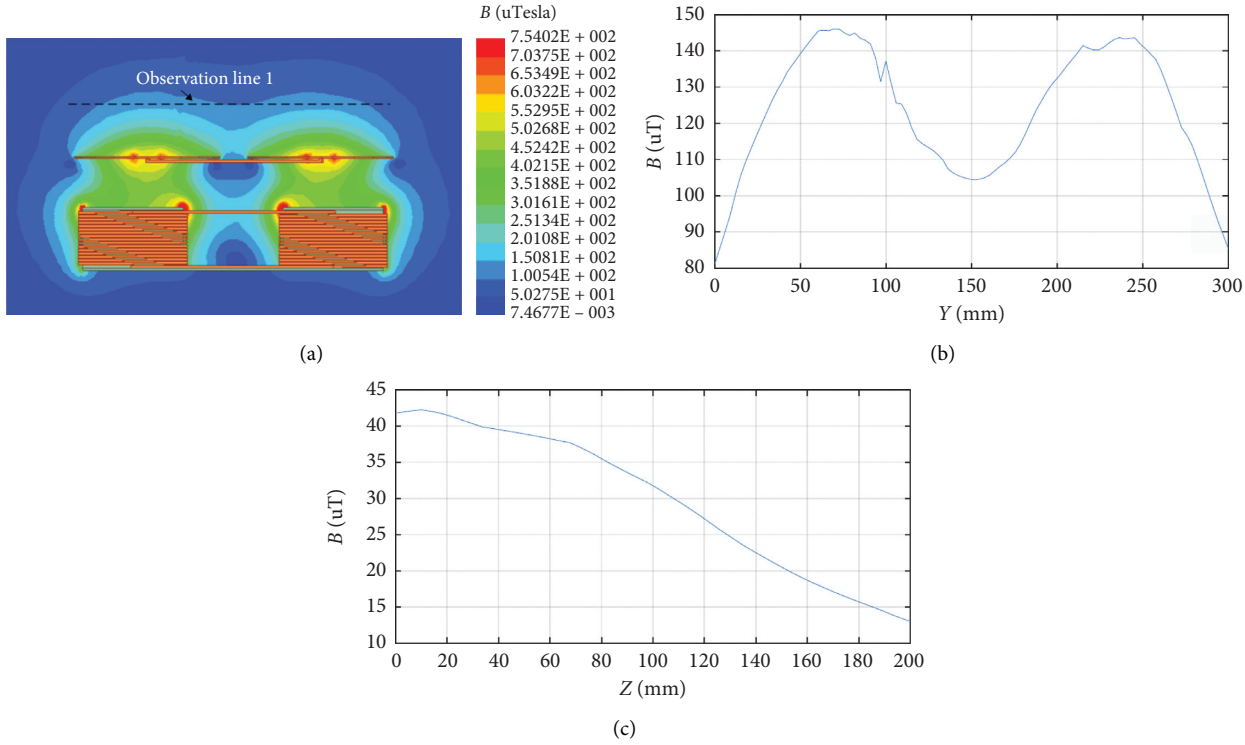

Figure 5: MF distribution curve during normal operation. (a) MF distribution of the *YOZ* plane. (b) Distribution of observation line 1. (c) Distribution of observation line 2.

3. Passive Shielding

3.1. Passive Shielding Mechanism. The wireless charging system can be shielded by magnetic materials. Common magnetic materials such as ferrite and iron-nickel alloy have the characteristics of high permeability and high saturation magnetic flux. The internal magnetic resistance is extremely small, and the magnetic flux circuit will be guided. It is possible to achieve the purpose of improving the MF distribution and weakening the local field strength through magnetic materials.

The alternating magnetic flux density **B** generated by the resonant coil will induce an electromotive force in the surrounding space, the induced electromotive force can form an eddy current in the conductor, and a counteracting MF will be generated to opposite to the original one. The effect of eddy current is shown in Figure 6. Accordingly, the eddy current can be used to reduce the leaked magnetic field.

3.2. Material Optimization of the Passive Shielding Device. In order to analyze the shielding effects of different magnetic materials, this paper selects iron-nickel alloy and ferrite shields for simulation. We add iron-nickel alloy and ferrite plates of the same thickness and same size 3 mm above the secondary side coil, and the magnetic induction intensity cloud diagram of the *YOZ* plane is as follows. Compared with the case without shielding in Figure 5, it can be seen intuitively that the magnetic induction intensity value on the upper and left sides becomes low, and the magnetic induction intensity value of the magnetic coupling area between the primary and secondary coils becomes high.

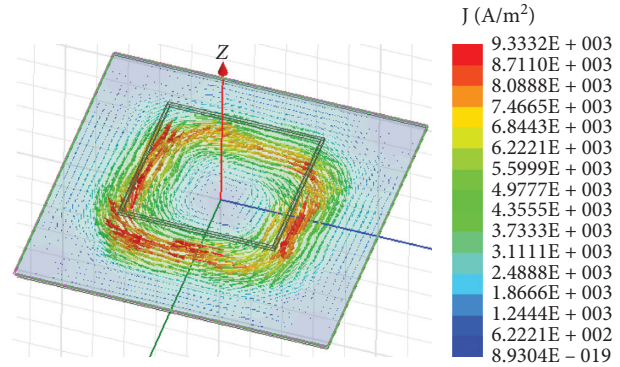

Figure 6: Eddy current effect.

The result in Figure 7 shows the shielding effect of the two materials. On observation line 1 above the secondary side, the ferrite shield plate represented by the blue curve does not change the MF change law of the coupling mechanism, while the iron-nickel alloy represented by the red curve fully reflects its advantage of high magnetic permeability. The level of magnetic induction on the observation line is greatly reduced. Considering that both materials can achieve a good shielding effect, and the metal nickel in the alloy shielding plate is more expensive, we choose a ferrite shielding plate that is cheaper and has a wider operating frequency range.

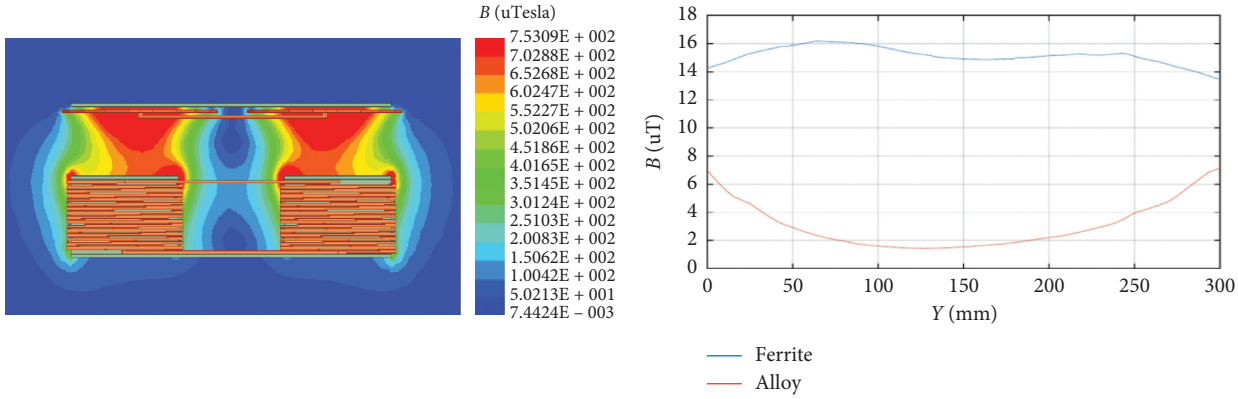

Figure 7: MF distribution curve in the presence of magnetic materials. (a) MF distribution of *YOZ* plane. (b) Distribution curve of observation line 1.

According to impact factors of the eddy current, when the resonance frequency, shielding plate thickness, volume, and relative permeability are the same, the conductivity becomes the determining factor of the eddy current loss. The higher the conductivity, the stronger the induced eddy current, and the more obvious the shielding effect. It is important to note that for the resonant wireless charging system, the intensity of the induced eddy current is closely related to the resonant frequency. When the frequency is too low, conductive metal materials cannot guarantee a good electromagnetic shielding effect.

Through simulation and comparison of the shielding conditions of aluminum and SUS306 (stainless steel) plates, it can be seen from Figure 8 that the MF in the coupling region of the primary and secondary coils is weaker than before shielding. Compared with the cloud image with magnetic material, the MF in the coupling region is greatly weakened. That is, when a metal material is used for shielding, the induced eddy current can weaken the main magnetic flux while canceling the leakage MF, resulting in the reduction of the self-inductance, mutual inductance, and coupling coefficient of the magnetic coupling mechanism.

It can be seen from the simulation results of the observation line that the shielding effects of the two metal shielding plates at 85 kHz frequency are very similar, and aluminum is the most abundant metal element in the earth's crust. It is cheap, light, and conductive. In addition, the eddy current loss is only 0.48597 W, which is much smaller than the 2.288 W in the stainless steel plate, so an aluminum plate is selected as the metal material.

After understanding the mechanism of magnetic materials and metal materials as the shielding layer, we try to combine the advantages of the two to form a composite shielding layer. We place an iron plate directly above the secondary side and then place an aluminum plate of the same size close to the iron plate to obtain the following cloud map distribution in Figure 9.

The composite shielding layer combines the effects of magnetic materials and metal materials, which not only enhances the MF coupling between the primary and the secondary coils and increases the coupling coefficient to 0.27593 but also reduces the leakage MF at the edge of the secondary coil, and the overall shielding effect is better.

In Figure 10, all values at observation line 1 have been reduced below standard, and the minimum value is 7 μT, which is 42.3% of the minimum shielding value of aluminum plate and 56.7% of the minimum value of ferrite shielding. On the vertical observation line 2, the standard value of magnetic flux density can be reached only 8.2 mm above the ground, and the exceeding range is 10.22% of the aluminum shielding.

In order to minimize the number of shielding materials and meet the expected shielding requirements, it is necessary to simulate and optimize shielding devices with different thicknesses. According to the material selection above, keeping the distance between the shielding layer and the secondary coil constant, the simulation analysis of ferrite plates and aluminum plates of different thicknesses is performed, and the results are as shown in Figure 11.

For the ferrite shielding board, the thicker the thickness, the more the MF lines pass through the board, the less the magnetic leakage, and the better the shielding effect. However, manganese-zinc ferrite is heavy. Considering that its shielding effect has met the standard value of ICNIRP-2010 when 2 mm is considered, a ferrite plate of this thickness can be used. The thickness has little effect on the shielding effect of the aluminum plate. Choosing a 0.5 mm aluminum plate can ensure the shielding effect and save material consumption.

3.3. Passive Shielding Position Optimization. On the one hand, considering that the Mn-Zn ferrite may have magnetic saturation, it is difficult to transport due to its brittleness and fragility, and it is not suitable to be too large, etc.; on the other hand, the magnetic induction intensity within the specified observation range already dropped below the standard owing to the ferrite, aluminum plates of different thicknesses were placed in the existing position, the MF on both sides of 33 mm near the edge of the secondary coil still

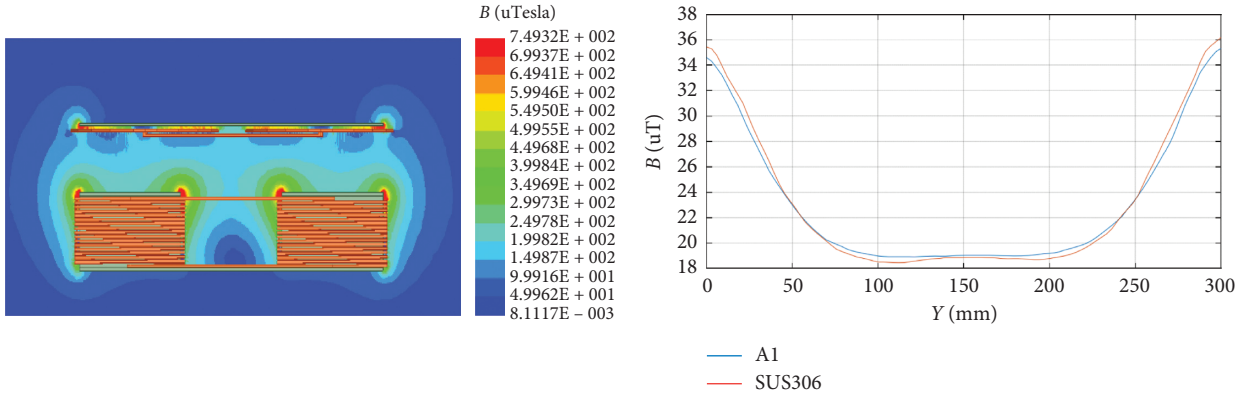

Figure 8: MF distribution curve in the presence of metallic materials. (a) MF distribution of *YOZ* plane. (b) Distribution curve of observation line 1.

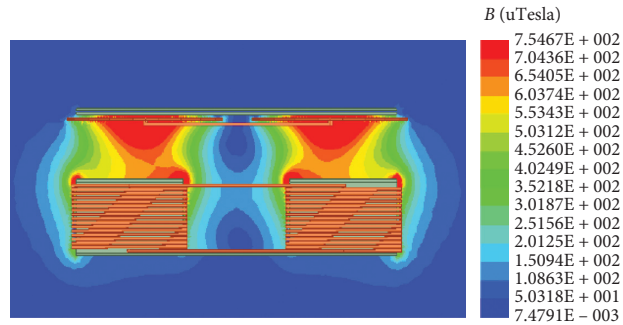

Figure 9: MF distribution of *YOZ* plane in the presence of composite materials.

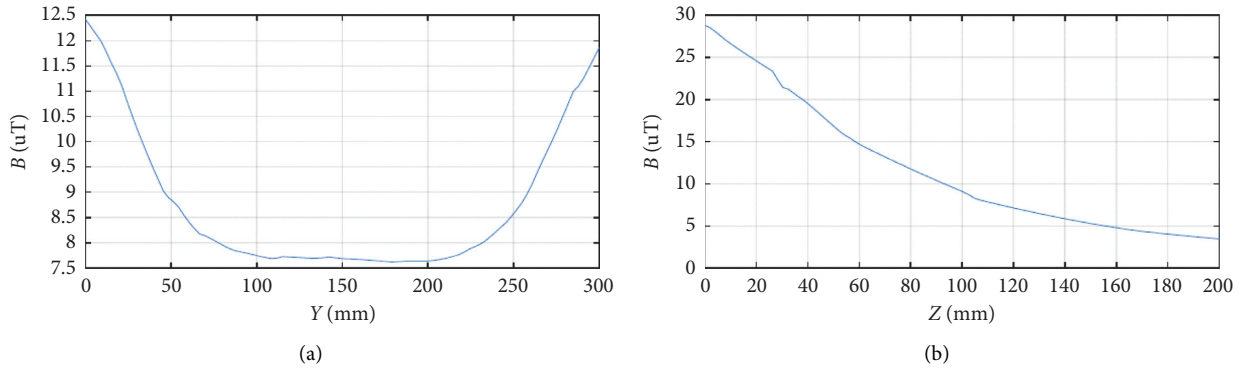

Figure 10: MF distribution curve in the presence of composite materials. (a) Observation line 1. (b) Observation line 2.

obviously exceeded the standard, and the MF within 80 mm on the ground did not fall below the safe value. Therefore, the use of an aluminum plate that is easy to cut should be considered as much as possible for shielding, and the position of the shielding plate should be optimized.

3.3.1. Secondary Side Horizontal Shielding. Based on the above conclusions on the shielding mechanism and thickness optimization of the aluminum plate, we can observe the relationship between the distance of the shield coil and the coupling coefficient, eddy current loss, and magnetic induction intensity of the system.

Table 1 shows the simulation data of the horizontal aluminum plate in different positions. As the distance between the aluminum plate and the coil increases, the coupling coefficient between the coils increases significantly, but at the same time, the shielding effect decreases slightly. Taking into account the transmission efficiency and shielding effect, 7 mm is selected as the distance between the aluminum shielding plate and the secondary coil.

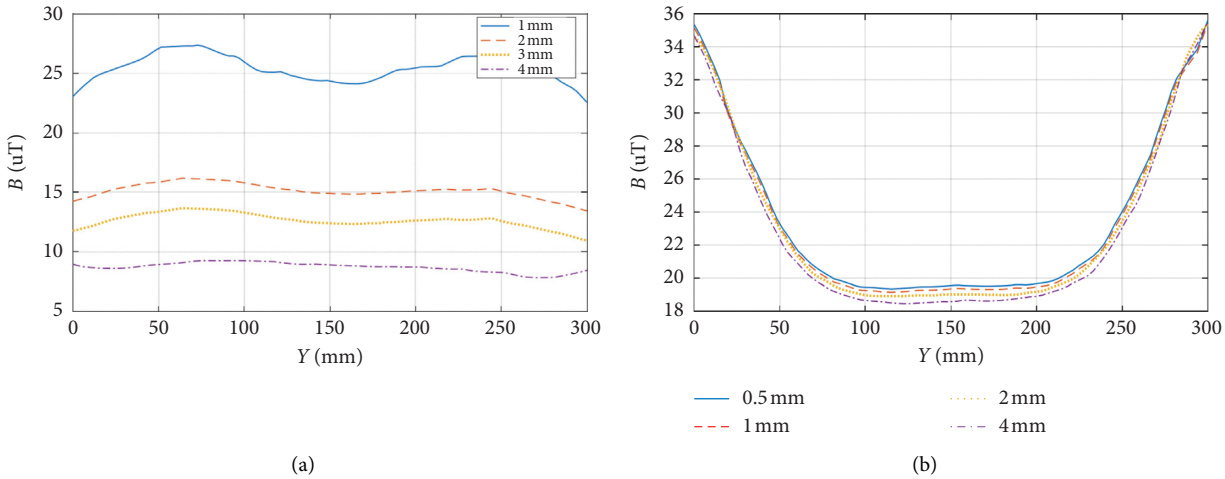

Figure 11: Shielding effect of different thickness plates. (a) Shielding effect of ferrite plates. (b) Shielding effect of aluminum plates.

Table 1: Simulation data of the horizontal aluminum plate on different positions.

Distance with the coils (mm)	k	Eddy current loss (w)	The range over the standard (mm)
3	0.054414	0.53951	78
5	0.073893	0.48597	80.2
7	0.090421	0.46328	83.8
9	0.10493	0.44639	87.6

3.3.2. Vertical Shield on Secondary Side. The inspection robot must move along the launching side track, so there is a certain air gap between the secondary side and the primary side. We choose aluminum plates with a length of 300 mm and a width of 20 mm and install them, respectively, on both sides of 20 mm from the secondary coil, as shown in Figure 12.

According to the simulation results, after installing the vertical shield, the range of the MF below the safe value in the space has not been significantly expanded. It can be seen that the passive shielding method is not suitable for vertical shielding on the secondary side of the magnetic coupling mechanism.

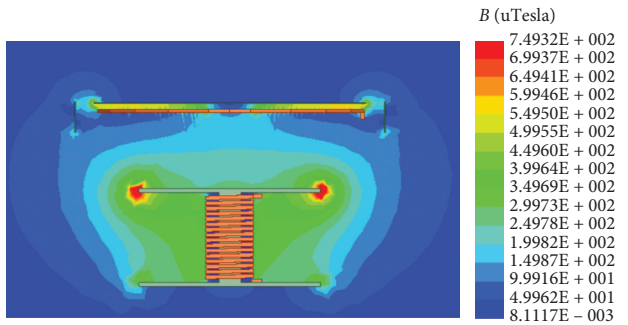

Figure 12: MF distribution of the *XOZ* plane with vertical shielding on the secondary side.

3.3.3. Horizontal Shielding on the Primary Side. Installing passive shielding devices on the primary side can also weaken the local MF strength. We place a 300 mm × 55 mm aluminum plate horizontally on the ground, keeping a distance of 40 mm from the primary coil, as shown in Figure 13.

On observation line 1 above the secondary side, the range below the safe value of the MF is 233.4 mm. On the vertical observation line 2 beside the secondary coil, the value of the magnetic flux induction drops to 27 μT, and the range exceeding the standard value is 2.39% smaller than the method with only the horizontal aluminum plate in the secondary coil. On horizontal observation line 3 beside the primary coil, the overstandard MF is also improved compared to the situation where only the secondary side shielding is applied.

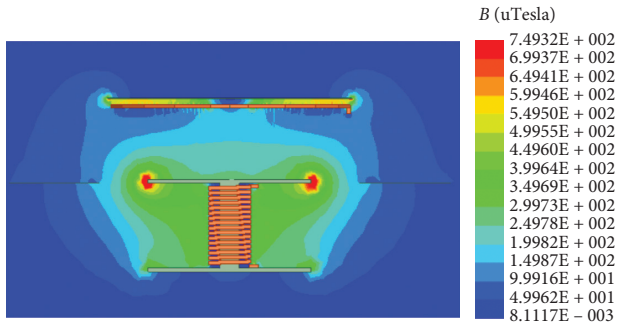

Figure 13: MF distribution of the *XOZ* plane with horizontal shielding on the primary side.

3.3.4. Primary Side Vertical Shield. An aluminum plate is placed vertically on the primary side, and the direction is parallel to the direction of movement of the inspection robot. The simulation results of the *XOZ* plane MF distribution map are shown in Figure 14.

On the observation line 1 300 mm above the secondary side, there is almost no change in the MF distribution, but on the observation line 2 on the right side of the secondary coil, it drops to 27 μT at 80.2 mm above the ground, and the overstandard range is lower than that when only the horizontal aluminum plate is added. On observation line 3 on the right side of the primary coil, the area where the MF intensity exceeds the standard is reduced by 8.31% compared with only the horizontal aluminum plate. It can be seen that this installation method can affect the distribution of magnetic induction in a wide range above the ground because it restricts the diffusion of the magnetic induction line to the surroundings on the primary side so that the direction becomes upwards along the aluminum plate, which is more directly related to the secondary coil. This method can also improve the coupling coefficient of the system.

4. Active Shielding

4.1. Active Shielding Theory. The difference between active shielding and passive shielding is that passive shielding uses conductive or magnetic materials to change the MF of the leakage area, while active shielding uses the MF generated by the energized coil to change the MF of the leakage area. Among them, the current of the active shielding coil or the magnetic flux formed by it should be at the same frequency as the resonance coil and have a phase difference of 180°. However, if the shielding coil is powered by an external source, it is difficult to sense and control the frequency and phase modulation process; on the other hand, it also reduces the overall efficiency of the system. This paper uses a series-type infinite shielding method, which can be used without any external source. Under the circumstances, active shielding is realized. The circuit impedance model is as shown in Figure 15.

From Figure 15, by changing the active suppression coil L_{SC} with secondary side coil L_{SM}, the relative position of the MF is generated by the resonant coil L_{SM}. The generated leakage MF is the same frequency and opposite phase, but the active shielding coil should be placed as far as possible outside the normal coupling path of the resonant coil to reduce the impact on the transmission effect. In order to study the influence of the added active suppression coil on the parameters in the original circuit, the current on the primary side is reduced to the secondary side using the ideal transformer rule, and the following Thevenin equivalent circuit of the secondary side is shown in Figure 15(b).

Due to the existence of an active shielding coil, the required matching capacitance becomes smaller. On the premise of achieving the purpose of offsetting the leakage MF, reducing the self-inductance L_{sc} of the suppression coil can reduce the impact on the matching capacitance in the original circuit. Based on this, we can optimize the structure and position of the active shielding coil.

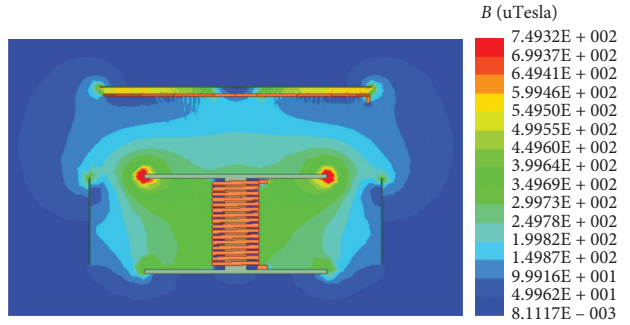

Figure 14: MF distribution of the *XOZ* plane with vertical shielding on the primary side.

4.2. Position Optimization of the Active Shielding Coil

4.2.1. Horizontal Suppression Coil on the Secondary Side. The above optimized results of passive shielding show that the MF values on both sides of the 33 mm edge of the secondary side coil still need to be reduced. Therefore, two horizontal suppression coils with opposite directions are added above the secondary side aluminum plate to offset the leakage MF on the left and right sides in different directions.

Figure 16 shows the connection method of the horizontal suppression coil in the simulation. There is still a distance of 50 mm between the secondary coil and the chassis of the patrol robot. Here, the number of turns of the suppression coil is tentatively set to 2. We change the height of the suppression coil to obtain the magnetic induction intensity change at the leftmost end of horizontal observation 1 above the secondary side coil.

The horizontal axis of Figure 17 represents the distance between the secondary coil and the active suppression coil. It can be seen that before 14 mm, the farther the distance is, the better the shielding effect is. Afterward, the shielding effect deteriorates because the influence of the reverse MF generated by the suppression coil on the observation point becomes stronger, which causes the MF at the observation point to increase. The effect of the number of turns of active suppression shielding effect is discussed hereinafter.

The result of Figure 18 shows that, within a certain range, the active suppression coil is farther from the main magnetic circuit; the more turns, the better the shielding effect. In this structure, the increase in the number of turns has a little effect on the MF of the lateral vertical observation line 2, but it has a significant impact on the upper horizontal observation line 1. When the number of turns is 4, the 50 mm above the receiving side is below the national standard limit. And its average value of 16.4 μT is 36.92% lower than the 26 μT of aluminum only. Therefore, we choose 4 as the number of turns of the suppression coil.

4.2.2. Vertical Suppression Coil on the Secondary Side. Previous studies have shown that the passive shielding and active horizontal suppression coils on the secondary side can hardly affect the magnetic induction intensity on the side observation line 2 of the robot, so we try to install a vertical

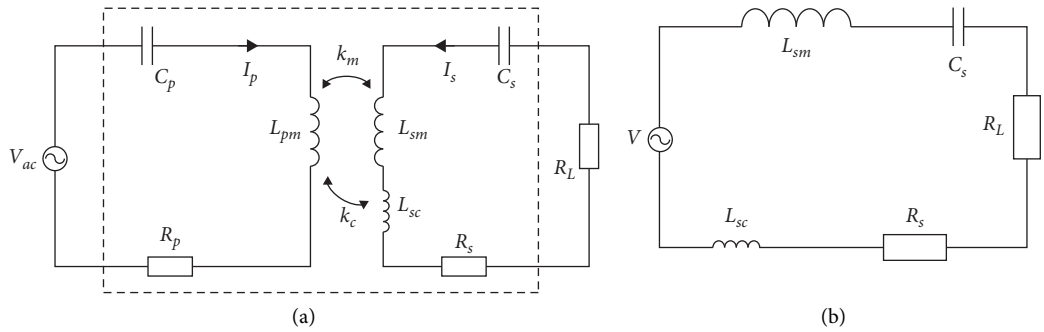

Figure 15: Topology models of active shielding. (a) Impedance model of active shielding. (b) The equivalent circuit diagram.

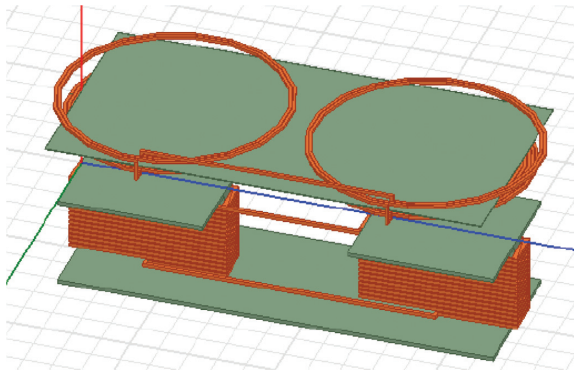

Figure 16: Connection method of horizontal suppression coil.

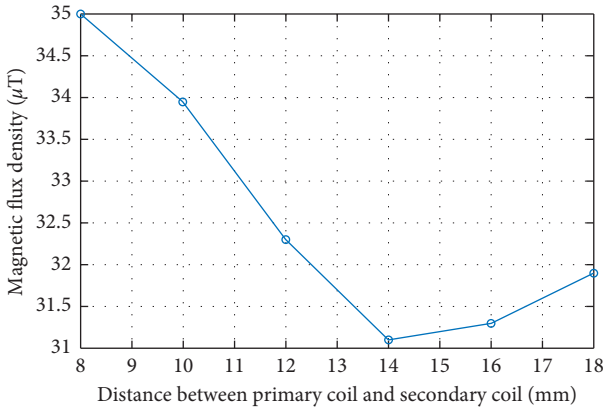

Figure 17: Magnetic flux density on the left side of observation line1.

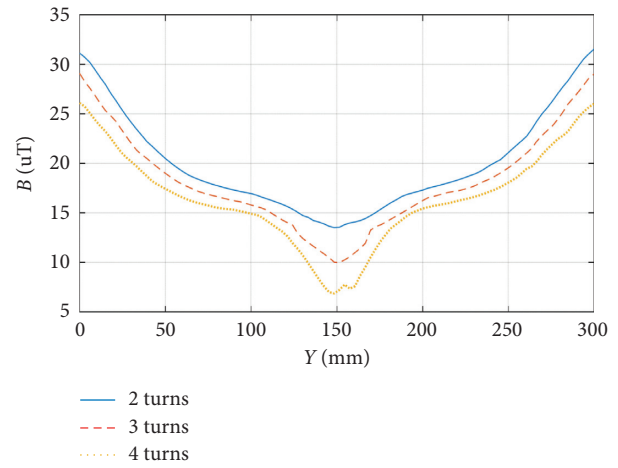

Figure 18: MF distribution curve of observation line 1.

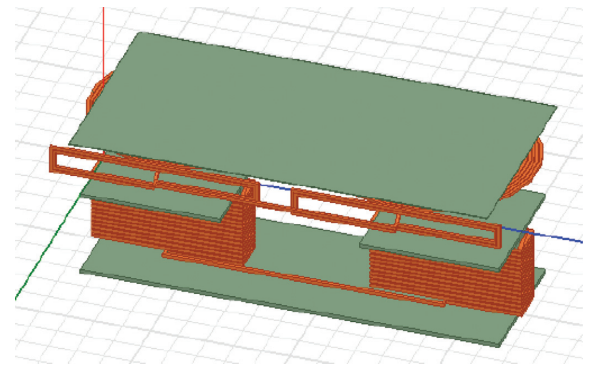

Figure 19: Connection method of vertical suppression coil.

suppression coil shown in Figure 19 to improve the MF distribution here.

In order to compare with the case of adding vertical shielding on the secondary side in passive shielding, the position, length, and width of the active suppression coil are kept consistent with the previous aluminum plate, while changing the number of the coil turns to suppress the corresponding design optimization.

It is reported in Figure 20 that with the change of the number of the active coil turns, the magnetic induction intensity on observation line 2 is significantly reduced. With 3 turns, it can be guaranteed that all above 51.3 mm on the ground falls below the standard value. The shielding effect of the vertical suppression coil under the same size is better than that of the aluminum plate. Therefore, it is more suitable for small magnetic coupling mechanism applications.

5. Experiment and Method Validation

5.1. Experimental Platform. Figure 21 shows our MF measurement experimental platform. The frequency-tracking high-frequency inverter power supply is selected, which can provide 85 kHz rated working power. The power supply does not need to accurately input the signal of the specified

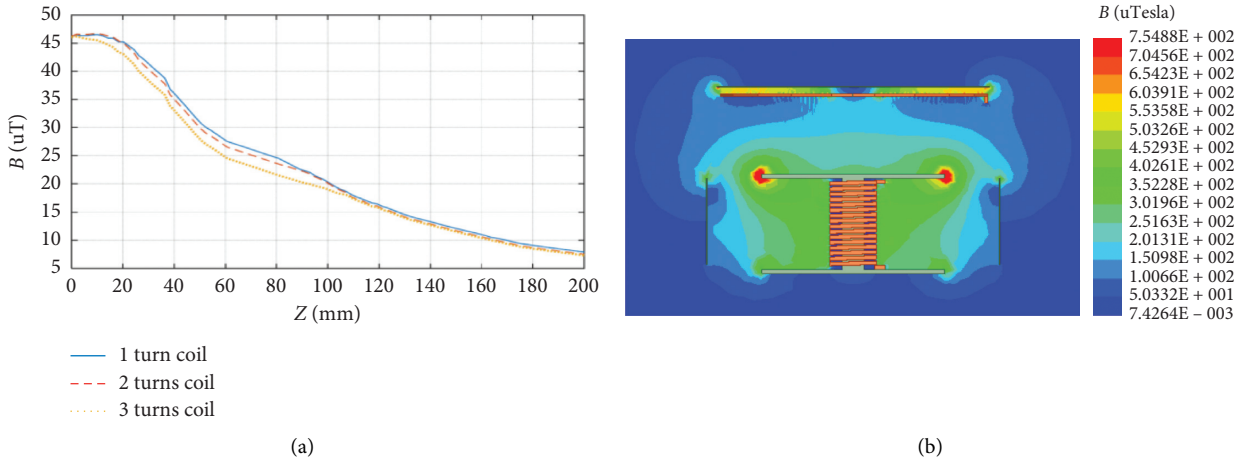

(a) (b)

FIGURE 20: Shielding effect of vertical suppression coil. (a) MF distribution of different turns of the coil. (b) MF distribution diagram of *XOZ* plane.

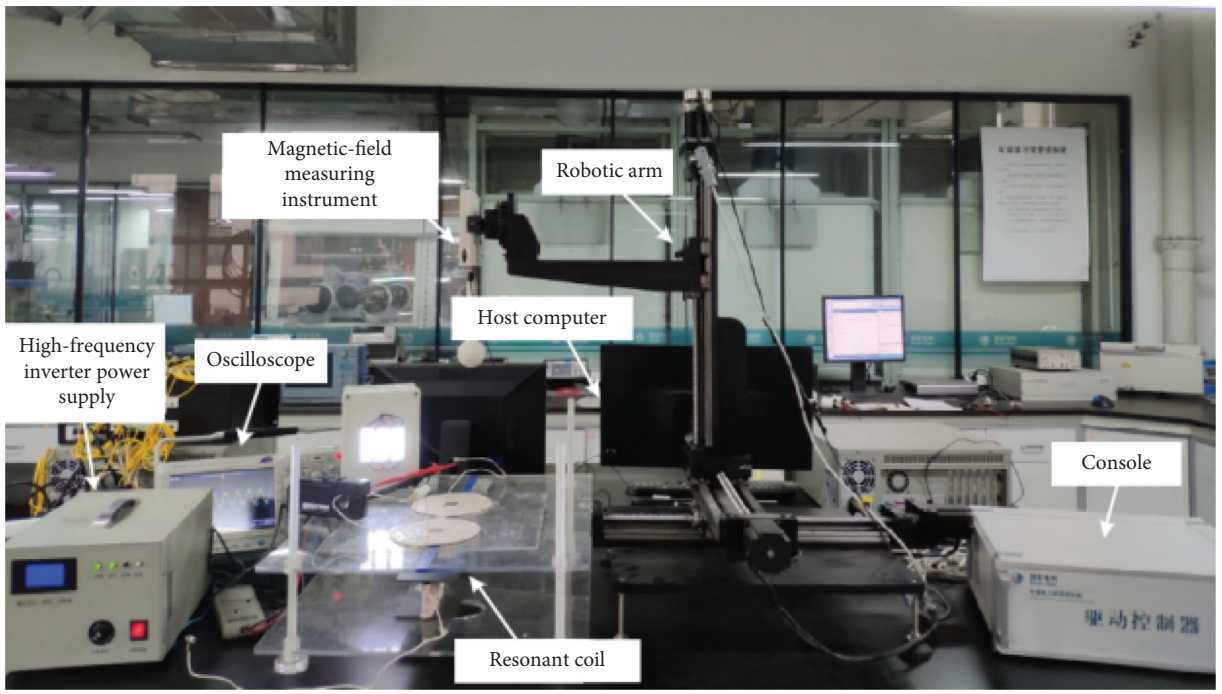

FIGURE 21: MF measurement experimental platform.

frequency and can be automatically adjusted to ensure that the system is always in resonance. This can avoid the situation that the output power and efficiency of the system are drastically reduced due to the shift of the resonance point when the system structure changes.

The resonant coil is wound according to the simulation model parameters. The coil wire adopts Litz wire with a specification of 0.2 mm × 75 mm strands, and the maximum fluid resistance value is 8.856 A. The wire diameter is 2 mm measured with a vernier caliper. The 75 strands of wires inside the coil are insulated from each other. When the current is applied, the stranded multistrand enameled wire can effectively suppress the skin effect and reduce the wire loss. The I-type magnetic core is spliced by manganese-zinc ferrite of different sizes. When splicing, attention should be paid to reducing the gap to prevent the distortion of the MF lines.

As the most critical part of resonance, capacitance needs to match the actual measured value of coil inductance. Here, the impedance analyzer NF ZGA5920 is used to accurately measure the self-inductance, and then the capacitance value is calculated through the resonance condition of the series compensation.

The received high-frequency energy is converted to DC through a rectifier module, and the load is composed of 72 LED bulbs. The load can be more directly observed experimental phenomenon when shielding device is added, and it will not affect the coupling state of the coil.

Table 2: The parameters of the experiment.

Parameters	Primary side	Secondary side
Frequency	85 kHz	
Distance	50 mm	
Real power	2.46 kW	1.968 kW
Self-inductance (sim)	360.81 μH	91.476 μH
Self-inductance	354.76 μH	94.7 μH
Resonant capacitance	10.1 nF	37 nF
Resistance	0.341 Ω	0.407 Ω
Number of turns	16 × 2	24 × 2

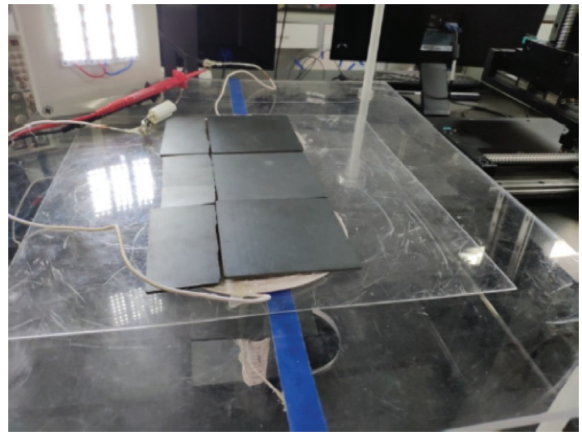

Figure 22: Position of magnetic material shielding.

5.2. Experimental Data and Analysis. Table 2 shows the electromagnetic configuration used in our simulation (sim) and experiment.

5.2.1. Magnetic Shielding Device Verification. First, we test the situation without a shielding device and with magnetic material above the secondary side. The magnetic material, manganese-zinc ferrite, is located 3 mm above the secondary coil and is spliced with a square core of 2 mm thickness. The position of the magnetic material is shown in Figure 22.

After setting the initial measurement position and the measurement length of the two axial directions on the host computer interface, we power on the wireless charging system to make it reach the resonance state. We use the host computer to drive the console and the robotic arm to make the three-dimensional MF measuring instrument collect the MF value on the specified plane and then output it through the connected USB interface to draw the following three-dimensional MF distribution map in Figures 23 and 24.

$X = 75$ mm in the X-Y measurement plane and $Y = 65$ mm in the Y-Z measurement plane correspond to observation lines 1 and 2, respectively. The test result of the measuring instrument shows that without any shielding, the maximum magnetic induction intensity at 50 mm above the secondary side can reach 140 μT, and the minimum value is 60 μT, far exceeding the corresponding ICNIRP-2010. After adding the ferrite shielding device, the MF values in the two measurement planes dropped sharply, the maximum drop in the X-Y measurement plane was 88.57%, and the maximum drop in the Y-Z measurement plane was 34.88%. In addition, the ferrite shielding device increases the system efficiency from 80.2% to 82.4%.

5.2.2. Metal Shielding Device Verification. As is shown in Figures 25 and 26, the experimental results are consistent with the simulation MF distribution law. The aluminum plate minimizes the central MF of the X-Y measurement plane, which is 85.71% lower than that without any shielding. The closer to the surroundings, the greater the MF value. Compared with the case without shielding, more than 85% of the area in the plane is replaced by the blue area below 25 μT, and the magnetic induction intensity of the test plane is basically up to the standard.

5.2.3. Active Shielding Device Verification. On the basis of passive shielding, two types of active suppression coils are added. The horizontal suppression coil selects 4 turns and is placed 14 mm above the secondary coil, as shown in Figure 27. The measured self-inductance is 12.93 μH; the vertical suppression coil selects 3 turns and places it. At 20 mm to the right of the secondary coil, the total length and total width of the two vertical suppression coils with opposite winding directions are consistent with the vertical aluminum plate on the secondary side, and the self-inductance is measured to be 4.13 μH. We connect the two active suppression coils to the circuit, respectively, and continue the measurement after the system is in resonance.

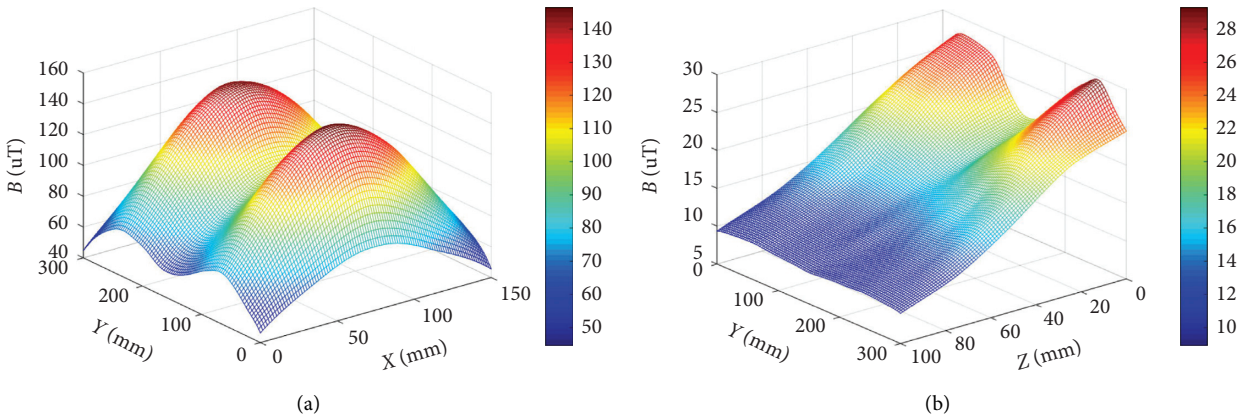

Figure 23: 3D MF distribution without shielding. (a) X-Y measurement plane. (b) Y-Z measurement plane.

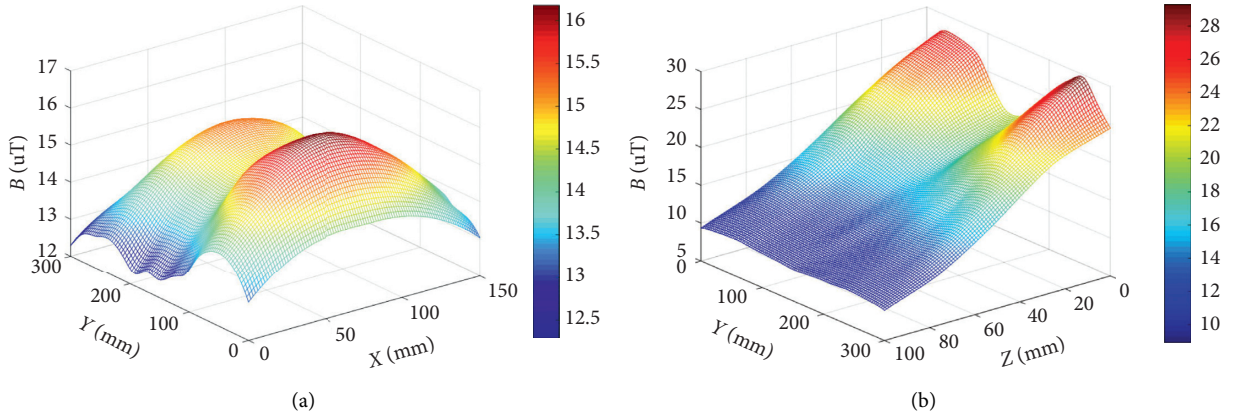

Figure 24: 3D MF distribution with magnetic shielding. (a) X-Y measurement plane. (b) Y-Z measurement plane.

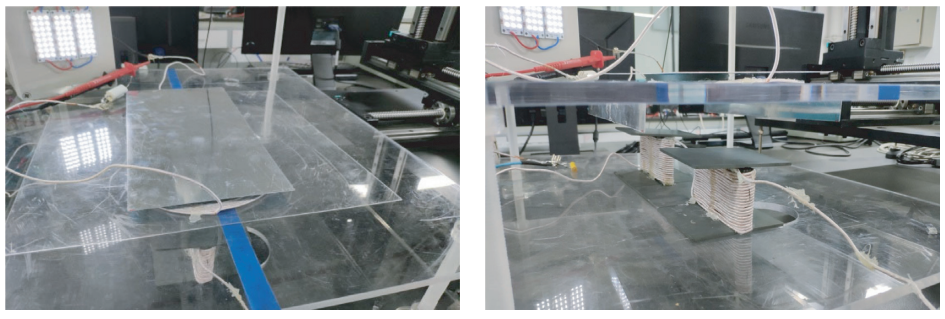

Figure 25: Position of metal material shielding. (a) 0.5 mm aluminum plate on the receiving side. (b) 2 mm aluminum plate on the receiving side.

The results in Figure 28 show that the active shield has a more significant shielding effect than the horizontal aluminum plate, which can reduce the magnetic induction intensity to a minimum of 8 μT, and the edge value of the plane also drops below the safe value. The Y-Z plane results show that the vicinity of the vertical suppression coil can be placed below the safe value, which ensures the electromagnetic safety of electronic equipment and staff in non-working areas for a long time. Through the measurement of the oscilloscope, it is found that the transmission efficiency has dropped from 80.2% without the shielding device to 77.6%, making the system efficiency slightly lower.

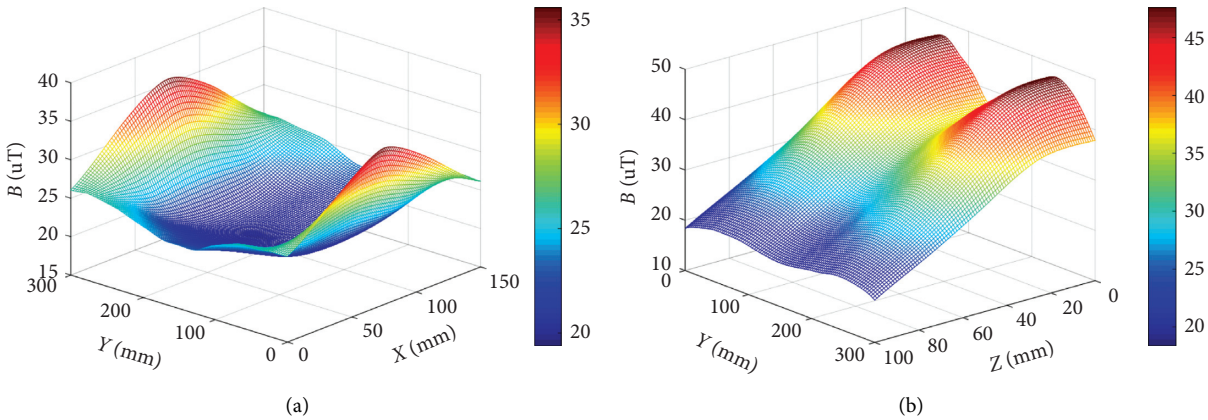

FIGURE 26: 3D MF distribution of X-Y measurement plane. (a) 0.5 mm aluminum plate on the receiving side. (b) 2 mm aluminum plate on the receiving side.

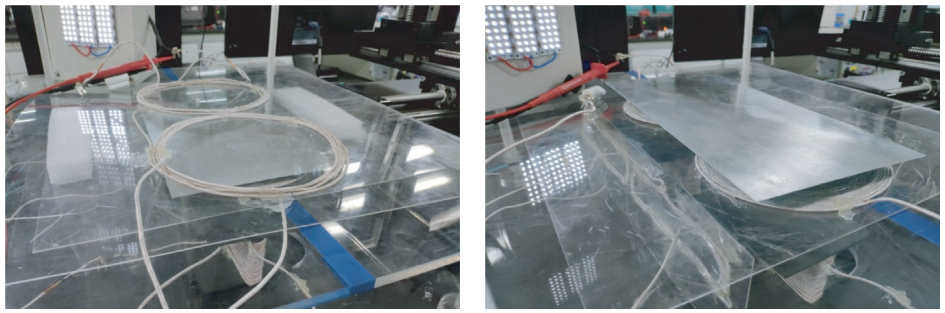

FIGURE 27: Physical picture of active shielding. (a) Horizontal suppression coil. (b) Vertical suppression coil.

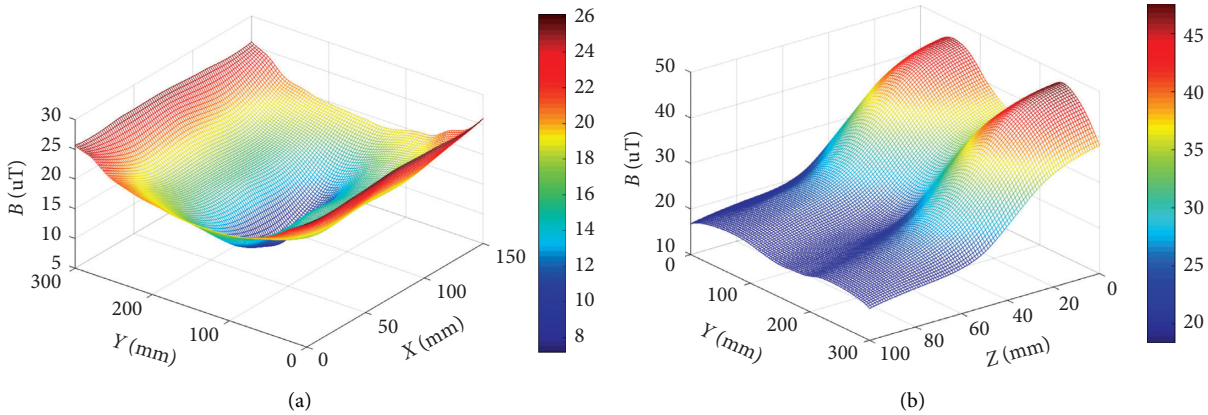

FIGURE 28: 3D MF distribution of the system with active shielding. (a) X-Y measurement plane. (b) Y-Z measurement plane.

6. Conclusions

In this paper, we proposed an electromagnetic shielding method combining passive shielding and active shielding. As a result of Maxwell simulation and experiment, it is confirmed that the shielding method significantly reduced leaked magnetic field by almost 85% for the WPT system with a decrease in efficiency by 2.6%. Moreover, the following conclusions can be drawn from our study:

(1) Passive shielding can achieve shielding effect on the primary or secondary sides of the WPT, but the shielding ability in the vertical direction is not as good as the active shielding, and a large area of

shielding board will hinder the mobility of the WPT system

(2) Magnetic material and conductive material have an opposite effect on coupling coefficient so that we can combine those two materials in passive shielding. But it should be pointed out that the thickness of ferrite has a great influence on the shielding effect, and the thickness of the aluminum plate has a little effect on the shielding effect, but all of them are positively correlated

(3) Under the same proportion of space, the MF weakening ability of active shielding is 34.06% higher than that of only passive shielding

(4) The secondary side is the best mounting position for active shielding

For future works, a more realistic multiphysical field model will be established to analyze the electromagnetic loss of the WPT system and the resonant frequency offset caused by the shielding design. In addition, the saturation phenomenon of the I-shaped core skeleton and optimizing its structure will be studied in further work.

Data Availability

The data that support the findings of this study are available on request from the corresponding author.

Conflicts of Interest

The authors declare that there are no conflicts of interest.

Acknowledgments

This work was supported by Joint Funds of the National Natural Science Foundation of China (U20A20305).

References

[1] P.-P. Ding, L. Bernard, L. Pichon, and A. Razek, "Evaluation of electromagnetic fields in human body exposed to wireless inductive charging system," *IEEE Transactions on Magnetics*, vol. 50, no. 2, pp. 1037–1040, 2014.

[2] C. Chen, X. Huang, and L. Tan, "Electromagnetic environment and security evaluation for wireless charging of electric vehicles," *Transactions of China Electrotechnical Society*, vol. 30, no. 19, pp. 61–67, 2015.

[3] G. Xu, C. Li, and J. Zhao, "Electro-magnetic environment safety study of wireless electric vehicle charging," *Transactions of China Electrotechnical Society*, vol. 32, no. 22, pp. 152–157, 2017.

[4] L. Zhai, G. Zhong, Y. Cao, G. Hu, and X. Li, "Research on magnetic field distribution and characteristics of a 3.7 kW wireless charging system for electric vehicles under offset," *Energies*, vol. 12, no. 3, p. 392, 2019.

[5] M. Mohammad, E. T. Wodajo, S. Choi, and M. E. Elbuluk, "Modeling and design of passive shield to limit EMF emission and to minimize shield loss in unipolar wireless charging system for EV," *IEEE Transactions on Power Electronics*, vol. 34, no. 12, pp. 12235–12245, 2019.

[6] H. Kim, C. Song, D. H. Kim et al., "Coil design and measurements of automotive magnetic resonant wireless charging system for high-efficiency and low MF leakage," *IEEE Transactions on Microwave Theory and Techniques*, vol. 64, pp. 383–400, 2016.

[7] Q. Zhu, Y. Guo, L. Wang, C. Liao, and F. Li, "Improving the misalignment tolerance of wireless charging system by optimizing the compensate capacitor," *IEEE Transactions on Industrial Electronics*, vol. 62, no. 8, pp. 4832–4836, 2015.

[8] M. Budhia, J. T. Boys, G. A. Covic, and C.-Y. Huang, "Development of a single-sided flux magnetic coupler for electric vehicle IPT charging systems," *IEEE Transactions on Industrial Electronics*, vol. 60, no. 1, pp. 318–328, 2013.

[9] A. Zaheer, H. Hao, G. A. Covic, and D. Kacprzak, "Investigation of multiple decoupled coil primary pad topologies in lumped IPT systems for interoperable electric vehicle charging," *IEEE Transactions on Power Electronics*, vol. 30, no. 4, pp. 1937–1955, 2015.

[10] V. De Santis, T. Campi, S. Cruciani, I. Laakso, and M. Feliziani, "Assessment of the induced electric fields in a carbon-fiber electrical vehicle equipped with a wireless power transfer system," *Energies*, vol. 11, no. 3, p. 684, 2018.

[11] A. Zaheer, D. Kacprzak, and G. A. Covic, "A bipolar receiver pad in a lumped IPT system for electric vehicle charging applications," in *Proceedings of the IEEE Energy Conversion Congress and Exposition (ECCE)*, pp. 283–290, Vancouver, Canada, September 2012.

[12] J. Kim, J. Kim, S. Kong et al., "Coil design and shielding methods for a magnetic resonant wireless power transfer system," *Proceedings of the IEEE*, vol. 101, no. 6, pp. 1332–1342, 2013.

[13] H. Hwansoo Moon, S. Sungkyu Kim, H. H. Hyun Ho Park, and S. Seungyoung Ahn, "Design of a resonant reactive shield with double coils and a phase shifter for wireless charging of electric vehicles," *IEEE Transactions on Magnetics*, vol. 51, no. 3, pp. 1–4, 2015.

[14] Y. Jing, B. Sun, and Z. Zhu, "Shielding effectiveness of infinite metal plate with finite thickness at oblique incident and arbitrary polarizations," in *Proceedings of the Conference on Environmental Electromagnetics (CEEM)*, pp. 241–245, Hangzhou, China, November 2015.

[15] S. Cruciani, T. Campi, F. Maradei, and M. Feliziani, "Active shielding design for wireless power transfer systems," *IEEE Transactions on Electromagnetic Compatibility*, vol. 61, no. 6, pp. 1953–1960, 2019.

[16] S. Cruciani, T. Campi, F. Maradei, and M. Feliziani, "Active shielding applied to an electrified road in a dynamic wireless power transfer (WPT) system," *Energies*, vol. 13, no. 10, p. 2522, 2020.

[17] J. Ren, B. Wang, and Z. Chen, "Density functional theory study of the magnetic properties of rare earth complexes: the magnetic coupling mechanism in YIII and GdIII complexes with nitronyl nitroxide," *Science in China Series B: Chemistry*, vol. 52, no. 11, pp. 1961–1968, 2009.

[18] T. Campi, S. Cruciani, V. De Santis, and F. Maradei, "Wireless power transfer (WPT) system for an electric vehicle (EV): how to shield the car from the magnetic field generated by two planar coils," *Wireless Power Transfer*, vol. 5, no. 1, pp. 1–8, 2018.

[19] Q.-F. Li, S.-B. Chen, W.-M. Wang, H.-W. Hao, and L.-M. Li, "Improving the efficiency of magnetic coupling energy transfer by etching fractal patterns in the shielding metals," *Frontiers of Information Technology & Electronic Engineering*, vol. 17, no. 1, pp. 74–82, 2016.

[20] Y. Kitano, H. Omori, T. Morizane, N. Kimura, and M. Nakaoka, "A new shielding method for magnetic fields of a wireless EV charger with regard to human exposure by eddy current and magnetic path," in *Proceedings of the International Power Electronics and Application Conference and Exposition*, pp. 778–781, Shenzhen, China, November 2014.

[21] J. Park and S. Ahn, "A novel shielding coil for electromagnetic field (EMF) reduction of wireless power transfer in laptop computer," in *Proceedings of the Wireless Power Transfer Conference IEEE, 2014*, pp. 235–238, Jeju Island, South Korea, May 2014.

[22] H. Kim, J. Song, and J. Kim, "Shielded coil structure suppressing leakage magnetic field from 100 W-class wireless power transfer system with higher efficiency," in *Proceedings of the IEEE MTT-S International Microwave Workshop Series on Innovative Wireless Power Transmission: Technologies, Systems, and Applications*, pp. 83–86, Kyoto, Japan, May 2012.

[23] International Commission on Non-Ionizing Radiation Protection, "Guidelines for limiting exposure to time-varying electric and MFs for low frequencies (1 Hz–100 kHz)," *Health Physics*, vol. 99, pp. 818–836, 2010.

[24] International Commission on Non-Ionizing Radiation Protection, "Guidelines for limiting exposure to electromagnetic fields (100 kHz to 300 GHz)," *Health Physics*, vol. 118, no. 5, pp. 483–524, 2020.